RESEARCH ARTICLE

Empirical evaluation of the strength and deformation characteristics of natural and synthetic gas hydrate-bearing sediments with different ranges of porosity, hydrate saturation, effective stress, and strain rate

Jun Yoneda[1]* , Kiyofumi Suzuki[2], Motoi Oshima[1], Michihiro Muraoka[2] and Yusuke Jin[1]

Abstract

Evaluating the mechanical properties of gas (primarily methane) hydrate-bearing sediments is essential for commercial production as a next-generation resource and understanding the global carbon cycle. Triaxial and uniaxial compression tests have been conducted on synthetic gas hydrate and natural core samples recovered from deep-sea beds using pressure coring techniques. The results show that four factors are vital in establishing the strength of hydrate-bearing sediments: hydrate saturation, effective confining stress, porosity, and strain rate. However, no study has evaluated these factors in a unified and quantitative manner, and even if the physical properties of the reservoir are known in detail from logging, predicting the strength has been challenging. In this study, pressure cores were drilled and recovered from the Eastern Nankai Trough in April 2018 after Japan's second offshore production test, and triaxial or uniaxial compression tests were performed on 12 pressure core samples brought back to the laboratory. The mechanical properties of the hydrate-bearing sediments were classified with previous obtained results from 53 pressure cores and 223 synthetic cores, and empirical equations for triaxial compressive strength and deformation modulus were proposed as functions of gas hydrate saturation, effective confining pressure, porosity, and strain rate. The obtained equations were found to correlate well with the experimental data and can predict the strength and deformation modulus from logging data.

Keywords Methane hydrate, Pressure core, Strength, Stiffness, Young's modulus, Triaxial test, Uniaxial test

*Correspondence:
Jun Yoneda
jun.yoneda@aist.go.jp
[1] National Institute of Advanced Industrial Science and Technology (AIST), Tsukisamuhigashi 2-17-2-1, Toyohira-ku, Sapporo, Hokkaido 062-8517, Japan
[2] National Institute of Advanced Industrial Science and Technology (AIST), Onogawa 16-1, Tsukuba, Ibaraki 305-8569, Japan

1 Introduction

Methane hydrate is an ice-like crystal that contains methane molecules inside a cage comprising water molecules (Sloan 2003). Owing to its ability to exist stably at low temperatures and high pressures, methane hydrate has been identified in nature at the bottom of deep seas and underground in permafrost regions. Two major natural gas hydrates morphologies exist, as follows: hydrate-bearing sediments composed of sand or silt with hydrate-filled pores and shallow type gas-hydrate in fine-grained muddy sediments appearing as chunks, nodules, veins, lenses, and fracture fillings. Such as hydrates

have the potential to become unconventional natural gas resources. Hydrates in sand are expected to be produced through conventional oil and natural gas drilling techniques, and methods are being developed to exploit this production. National projects for methane hydrate development have been launched in various countries since the 2000s, which have included exploration, coring, and field production tests. Depressurization, currently the most promising methane hydrate production method (Kurihara et al. 2008; Nagao 2012; Yamamoto and Nagakubo 2021), involves drilling a well in a reservoir where hydrate exists, using a pump to depressurize the in situ formation pressure (pore pressure) to pressure and temperature conditions outside of hydrate stability, decomposing the hydrate into methane gas and water, and retrieving the products from the well. During this process, solid methane hydrate, which has its own strength (Durham et al. 2003), is converted into liquid water and gaseous methane, resulting in reduced strength. Furthermore, in the example of Nankai Trough, as the depressurization method reduces the pore water pressure from approximately 13 MPa to the bottom hole pressure of 3 MPa, maximizing gas productivity, there is a concern that the effective stress born by the soil skeleton will increase, resulting in consolidation. As large frictional forces could occur between the well and formation, understanding the mechanical properties of the formation is necessary to evaluate the integrity and survivability of the resident production wells (Shin and Santamarina 2016; Yoneda et al. 2018). When considering the global glacial cycle, some studies have considered consider methane hydrate decomposition as a trigger for large-scale submarine landslides (Paull et al. 2007; Elger et al. 2018). Therefore, assessing geohazards caused by methane hydrate is critical for geoscience researchers, as methane released into the atmosphere is a greenhouse gas.

More than 200 triaxial compression tests have been performed using synthetic gas hydrates (Yun et al. 2007; Miyazaki et al. 2011a, b; Hyodo et al. 2005, 2013a, b, Masui et al. 2005). Yun et al. (2007) performed triaxial compression tests on artificial samples with tetrahydrofuran (THF) hydrate to show the effects of hydrate saturation (hydrate occupancy in the pore space) on strength and deformation properties. Masui et al. (2005), Miyazaki et al. (2011a, b), and Hyodo et al. (2005, 2013a, b) conducted triaxial compression tests for synthetic methane hydrate-bearing sediments to determine the effects of hydrate saturation under various drainage conditions and effective confining pressures. Miyazaki et al. (2010) proposed an empirical equation to estimate the strength from confining pressure and hydrate saturation. In this scenario, hydrate was formed from moist sand by injecting high-pressure methane gas (excess gas method) and replacing the methane gas with water. Their results showed good correlation with the natural core samples from the Nankai Trough under hydrate saturations of less than 40% (Masui et al. 2007). In studies of synthetic hydrate-bearing sand, the increase in strength caused by the presence of hydrates was assumed to be reflected in the apparent cohesion, and the friction angle was considered to be constant (Waite et al. 2009).

In the past decade, advancements in pressure core technology have enabled the recovery of natural gas hydrate-bearing sediments for analysis without incurring pressure loss; furthermore, triaxial compression testing of natural cores has been realized, leading to a better understanding of hydrate mechanical properties (Priest et al., 2015, Yoneda et al. 2015a, 2017, 2019a). In addition, cores collected from the Nankai Trough (Yamamoto 2015), Indian Ocean (Collett et al 2019), and Gulf of Mexico (Flemings et al 2020) have also been tested, and equations have been proposed to estimate the strength from the effective confining pressure and hydrate saturation (Yoneda et al. 2017), as well as examine the dependency of the strength on the strain rate (Yoneda et al. 2022). Priest and Hayley (2019) compared previous results from synthetic and natural samples to estimate how the morphology is affected by differences in hydrate formation processes and carefully explained the dependence on hydrate saturation, effective confining pressure, and clay content. Despite this progress in the understanding of mechanical properties, the equation used to estimate the strength in previous studies could not be used directly in the present numerical simulations (Kimoto et al. 2010; Rutqvist et al. 2009; Klar et al. 2013; Yoneda et al. 2018), as they require the strength of hydrate-free sediments. Furthermore, parameters for the deformation modulus, primarily used in simulations of ground deformation associated with hydrate production, are challenging to obtain owing to a lack of proposed datasets. In this study, pressure cores were recovered in the same area in which the second offshore production test was conducted in the Nankai Trough in April 2018 (Yamamoto et al 2019, 2021), and triaxial or uniaxial compression tests were performed on 12 pressure core samples at the onshore laboratory. Subsequently, the mechanical properties of the hydrate-bearing sediments were investigated from 309 test results, which include results from previous studies, and strength predictions were made based on the gas hydrate saturation (S_h), strain rate (R_{ea}), porosity (n), and effective confining pressure (σ_c'), parameters, on which the strength is highly dependent. In addition, the proposed equation is verified by comparing the predictions of strength (q_{max}) and deformation (elasticity) modulus (E_{50}), using logging data along with laboratory test results.

2 Materials and methods

Two coring wells (AT1-CW1 and AT1-CW2) were drilled in March and April 2018 after the completion of the second offshore production test in the Daini–Atsumi Knoll of the Nankai Trough in May–June 2017 (Yamamoto et al. 2021). The drilling vessel CHIKYU performed the coring, using a high-pressure–temperature corer (HPTC) III developed by JOGMEC (Nishioka et al. 2018). AT1-CW1 was drilled 10 m south of the P2 production well, and AT1-CW2 was drilled approximately 20 m west of the P3 production well at a location less affected by production testing to confirm the impact of production (Fig. 1). During production in the testing of well P3, which was closely located to CW2, the pressure was reduced from 12 to 6 MPa (Yamamoto et al. 2021). Two

weeks later, a depressurization of approximately − 1 MPa was observed in the hydrate layer of monitoring well MT3, which is approximately 20 m away (Ouchi et al. 2022). Similarly, CW2 was also approximately the same distance from MT2, and the impact of the production was an increase of approximately 1 MPa in effective stress. Here, the methane hydrate in CW2 had not yet begun to dissociate. In general, the strength of granular materials tends to increase when they undergo compression (increased effective stress) because of an increase in bulk density. For an effective stress increase of 1 MPa, the impact on the mechanical properties of the hydrate-bearing sandy layer is inferred to be small, as stress conditions are considered to be within the elastic region, based on past research (Yoneda et al. 2019b; Fang et al. 2021). This
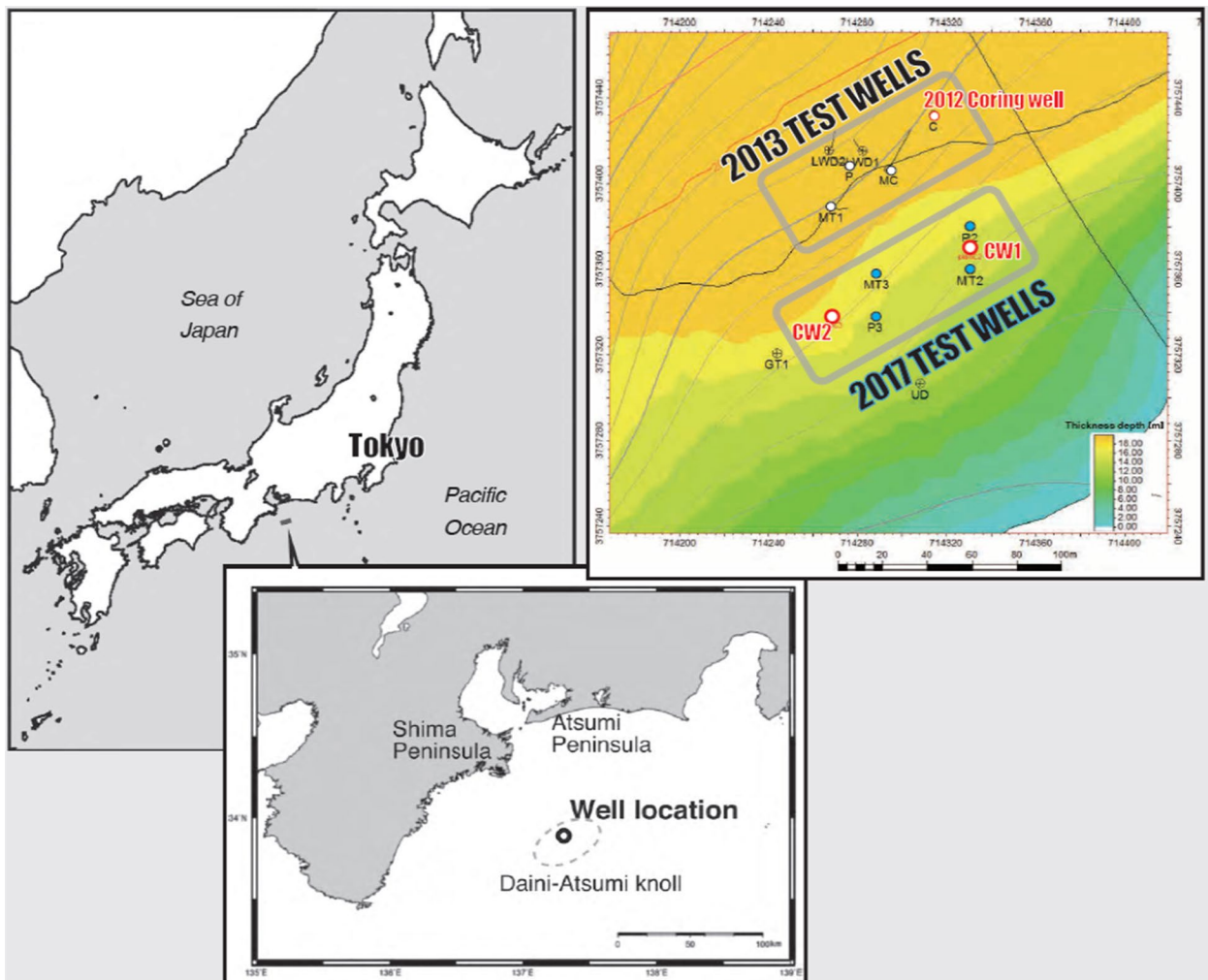

Fig. 1 Coring wells (CW1 and CW2) map at the AT1 site at the Eastern Nankai Trough [Reprinted from Yamamoto et al. 2019, Fire in the ice (Newsletters of National Energy Technology Laboratory of U.S. Department of Energy.)] The wells, named P, P2, and P3 for the gas production tests carried out in 2013 and 2017, are located on the Northwest slope of the Daini–Atsumi Knoll. The sand-dominant turbidite sequences contain gas hydrate, which are described as pore-filling and/or load-bearing type morphology

study used samples from the AT1-CW2 well, obtaining pressure cores with an average length of cores of 2.5 m. This coring was performed 25 times (runs). During the coring, the pressure inside the core was maintained at or above the borehole pressure in 23 of the runs. The pressure in the remaining two runs were slightly decreased, but within the hydrate stability boundaries. Thus, approximately 100% of the pressure cores was successfully performed, and 50.35 m of pressure core was recovered from the hydrate-concentrated zone at depths of 1286.5–1343.7 m and 1356.6–1362.7 m with a high recovery rate of 76%. The measured depth represents the water depth plus height of the rotary table, which is a reference level: rotary table 28.5 m, seabed 994.5 m. The X-ray images, P-wave velocities, and gamma-ray bulk densities of the recovered pressure cores were measured using a pressure core analysis and transfer system (Schultheiss et al. 2006) onboard the drilling vessel after examining the pressure–temperature history. Furthermore, three types of sorting were performed with onboard Pressure core Nondestructive Analysis Tools (PNATs) (Yoneda et al. 2015a, b; Jin et al. 2016), namely quantitative degassing, cryo core, and storage chamber. In this analysis, 14.6 m of high-quality

cores was stored in a pressure chamber and transported to the Hokkaido Center of AIST Sapporo. X-ray images, P-wave velocity measurements, and gamma-ray bulk density tests using PNATs were performed on the cores transported to the laboratory, confirming that no disturbances or other significant changes occurred owing to transportation.

Figure 2 shows the results of the wireline logging performed after coring and the various physical properties of the cores analyzed in this study. Table 1 shows the sample list for this study. The core grain size distribution that was chosen for the mechanical tests is shown in Fig. 3. A laser-based grain size analysis [Microtrac MT3300 EX (Nikkiso Co. Ltd.)] was conducted with the same technique used using in Ito et al. (2015), with the results expressed as volume percentages. The sand and mud alternation of the turbidite layer was 0.5–1 m at 1290–1320 m, and the sand layer at 1320–1380 m was thicker. The depositional age in the gas hydrate-reservoir sediments was 0.45–0.85 Ma (Egawa et al. 2015). The P-wave velocities at 1340–1345 m were greater than 3000 m/s in both the logs and cores. The maximum methane hydrate saturation (S_h) was approximately 80% based on
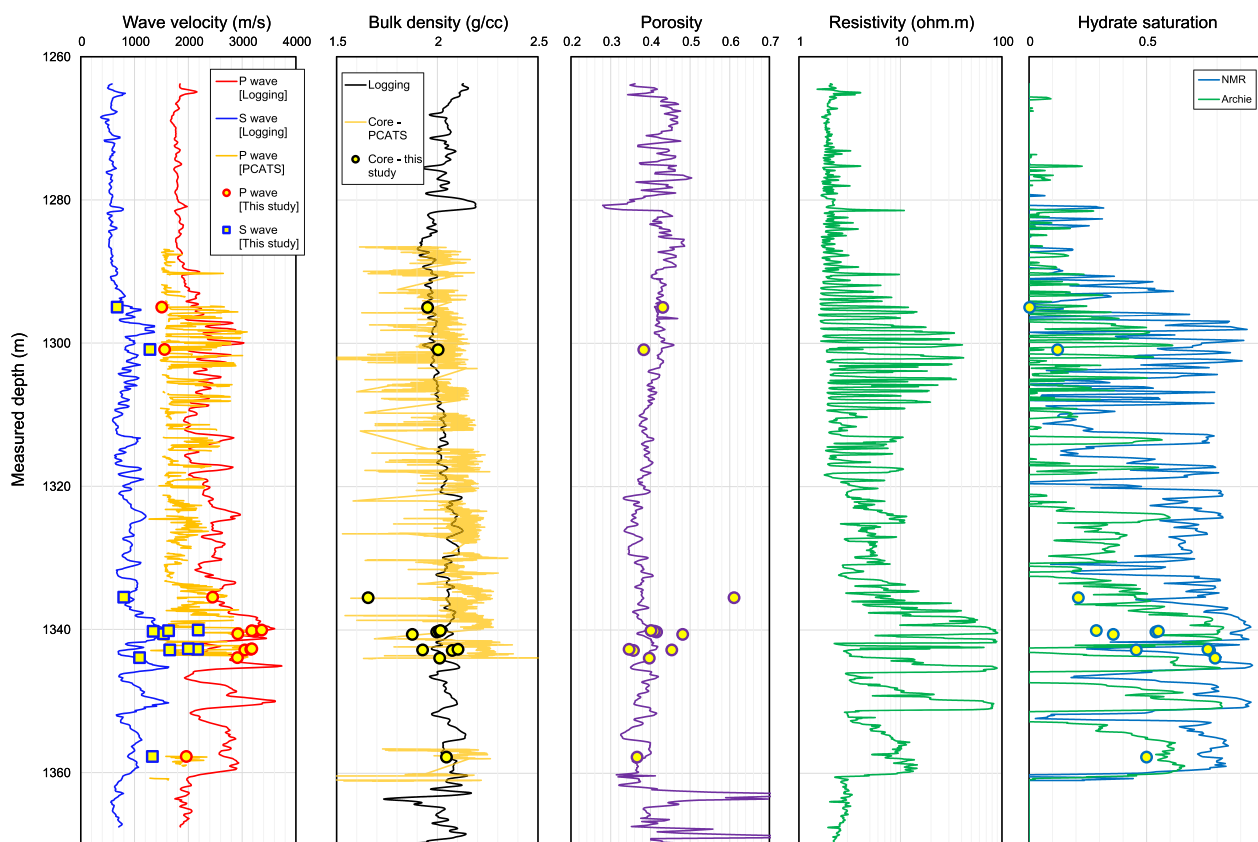

Fig. 2 Results of logging and core analyses. Logging data were acquired by JOGMEC. (Yamamoto et al. 2019, Ouchi et al. 2022). P- and S-wave velocities, bulk density, porosity, resistivity, and hydrate saturation are shown

Table 1 Core sample list

Sample ID:	Core top (m) measured depth Seabed: 994.5 m Rotary table: 28.5 m	Porosity *n*	Hydrate saturation S_h (%)	Test type	Strain rate: % Rε_a	Effective confining pressure: (MPa) σ_c'	Mean particle size: (um)
AT1-CW2-4P-2(43.5–52.5)	1295.25	0.432	0.3	Triaxial CU	0.01–0.05	1.6	6
AT1-CW2-6P-2a(5–12)	1300.88	0.454	9.1	Uniaxial	1	0	9
AT1-CW2-20P-2a(209–218)	1335.56	0.611	21	Uniaxial	10	0	92
AT1-CW2-22P-3(31–40.7)	1340.07	0.402	55	Triaxial CD	0.0001–0.001	2.0	88
AT1-CW2-22P-3(40.7–50.2)	1340.16	0.410	55.1	Uniaxial	0.0001–0.001	0	88
AT1-CW2-22P-3(50–60)	1340.26	0.416	54	Triaxial CD	0.01–0.1	2.0	77
AT1-CW2-22P-3(85–93)	1340.69	0.482	35.9	Uniaxial	0.0001–0.001	0	39
AT1-CW2-23P-2b(25–33)	1342.69	0.421	54.9	Uniaxial	0.01	0	88
AT1-CW2-23P-2b(33–41)	1342.77	0.458	39.7	Uniaxial	0.25–1	0	85
AT1-CW2-23P-2b(41–49)	1342.85	0.479	50.3	Uniaxial	0.01–0.1	0	85
AT1-CW2-23P-3b(56.2–66)	1343.93	0.466	59.1	Uniaxial	10	0	85
AT1-CW2-24P-1(5–13)	1357.74	0.439	36.6	Uniaxial	1	0	53
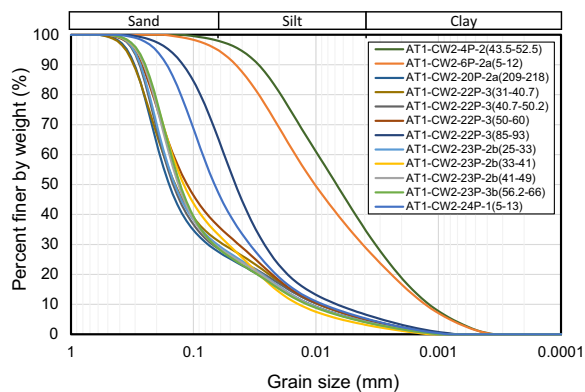
Fig. 3 Grain-size distribution curves for the core samples

the logging data. Of the sand layer samples, 10 were in good shape with high P-wave velocities and no cracking exhibited. Two samples [AT1-CW2-4P-2(43.5–52.5) and AT1-CW2-6P-2a(5–12)] were used to determine the mechanical strength of the muddy portion of the alternating sand and mud layers, with a total of 12 samples evaluated. An analysis plan was developed based on X-ray computed tomography (CT) images, P-wave velocity, and gamma-ray density data from pressure cores stored in 1.2 or 0.35 m pressure chambers and cut to 10 cm in length for testing. The cut core samples were loaded into a conveyance chamber and connected to the transparent acrylic cell triaxial testing (TACTT) system (Yoneda et al. 2013a, 2015a, b). Figure 4 shows the TACTT schematic diagram. In this system, the core sample is inserted into the rubber sleeve of the triaxial chamber and is ready for testing. The temperature and pressure are constantly monitored, with the methane hydrate maintained within
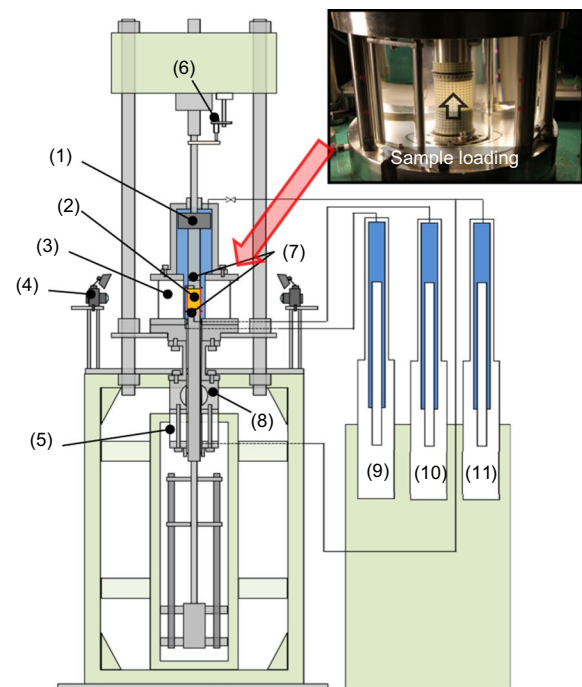
(1) Load cell (2) Core sample (3) Transparent acrylic cell (4) Camera
(5) Conveyance chamber (6) Displacement transducer
(7) Top cap & pedestal with piezo elements (8) Ball valve
(9) Syringe pump for upper bound of sediment
(10) Syringe pump for lower bound of sediment
(11) Syringe pump for cell pressure

Fig. 4 Diagram of transparent triaxial acrylic cell testing (TACTT) system

its stability boundaries. A syringe pump is connected to the top and bottom of the specimen after installation to monitor the pore fluid flowing in and out of the

specimen. Cell (confining) and pore pressures are controlled for the triaxial compression tests to apply an effective confining pressure. Outside the acrylic triaxial cell, eight cameras are used to measure the specimen's initial volume and volume changes using image processing. The top cap and pedestal above and below the specimen contain hollow cylindrical-shaped piezo-crystals that allow the vertical measurement of the P- and S-wave velocities of the core sample. When performing uniaxial compression tests, the confining and pore pressure bypasses are opened, and compression is performed with zero effective confining pressure. In this study, sand layer samples were subjected to drained conditions, whereas mud layer samples were subjected to undrained conditions. Both

tests were conducted at a temperature of 10 °C and water pressure of 10 MPa. As methane hydrate-bearing sediments are dependent on the strain rate, here, alternating strain rates were used for the axial loading, permitting the acquisition of the stress–strain curves corresponding to the strain rate.

3 Results

Figure 5 shows the uniaxial compression results for alternating strain rate compression tests. In this figure, the interpolated stress–strain relationship for each strain rate is illustrated as dotted and dashed lines. The strain rates in Fig. 5A and B correspond to 0.0001%/min and 0.001%/min. Deformation occurs over several months
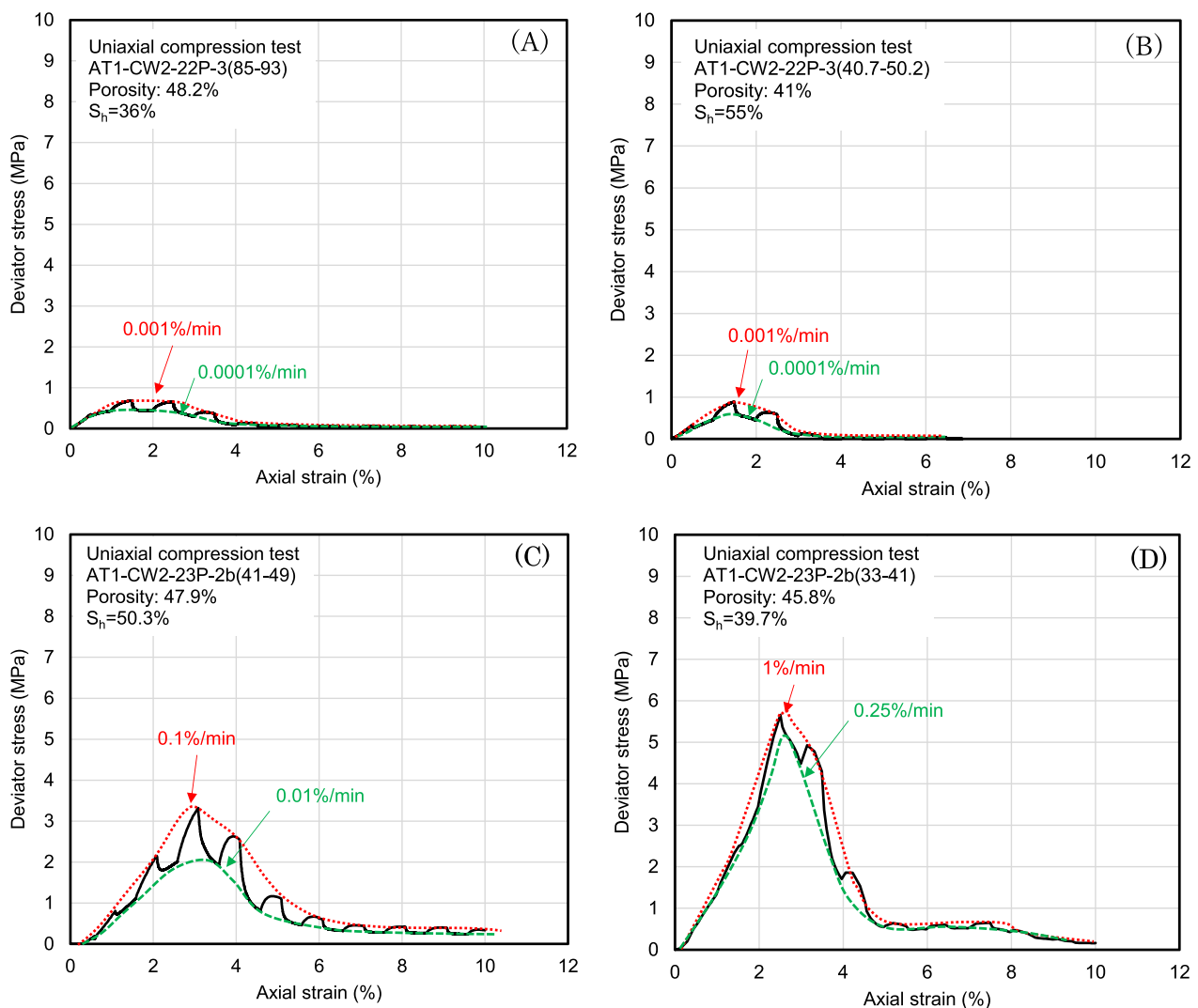

Fig. 5 Alternating strain rate uniaxial compression test results. **a** Core sample AT1-CW2-22P-3(85–93). Compression strain rate $R\varepsilon_a = 0.001\%$/min to 0.0001%/min. **b** AT1-CW2-22P-3(40.7–50.2). Compression strain rate $R\varepsilon_a = 0.001\%$/min to 0.0001%/min. **c** AT1-CW2-23P-2b(41–49). Compression strain rate $R\varepsilon_a = 0.1\%$/min to 0.01%/min. **d** AT1-CW2-23P-2b(33–41). Compression strain rate $R\varepsilon_a = 1\%$/min to 0.25%/min

at 0.0001%/min, a prolonged loading rate for laboratory testing, and this has not been tested in previous studies. However, such a rate is assumed to be similar to real-field deformation, in which depressurization is applied to the reservoir over periods of days to months. The compressive strength of 0.0001%/min is approximately half that of 0.001%/min. The sample in Fig. 5B has a higher peak strength than in Fig. 5A owing to higher hydrate saturation and lower porosity. Figure 5C shows the compression results for 50.3% hydrate saturation at 0.1%/min and 0.01%/min. Figure 5D shows the compression results for 39.7% hydrate saturation at 1%/min and 0.25%/min. As the strain rate increases, the strength increases. Sand has little strain rate dependence compared to hydrate-bearing sediments (Miyazaki et al. 2007). Meanwhile, studies have reported the strain rate dependence of hydrate sediments on synthetic methane hydrate-bearing sediments (Miyazaki et al. 2007). Hydrates have also been found to be strain rate dependent (Durham et al. 2003). Strain rate alternating compression tests have previously been conducted on a few pressure cores collected offshore India and in the Gulf of Mexico, confirming, along with the present results, that natural hydrate deposits are strain rate dependent (Yoneda et al. 2019a, 2022).

Figure 6 shows the results of two triaxial compression tests conducted at strain rates of 0.1, 0.01, 0.001, and 0.0001%/min. Effective confining pressure was applied as the stress estimated in situ ($\sigma_c' = 2$ MPa). Two samples were taken from a single sand layer with near-equal porosity and hydrate saturation. Strain rate dependence can be observed under triaxial stress conditions. Volume change is correlated with the stress–strain relationship, confirming a shift from compressive to dilative behavior for strain softening in the case of sediments with higher compression rates [AT1-CW2-22P-3(50–60)]. Sediments with smaller compression rates [AT1-CW2-22P-3(31–40.7)] exhibited an initial change in volume followed by constant volume, a result that was correlated with the convergence of deviator stress. Thus, strain rate dependence and hydrate considerably influence the deformation of hydrate-bearing sediments.

Because sand does not have cohesion, the unconfined compression test results can be considered a direct effect of increased strength owing to the presence of hydrate. The fact that the deviator stress is zero toward the end of the compression test (Fig. 5a and b) implies that the measurement of a deviator stress in the early stages of compression is a direct strengthening effect of the presence of hydrates. The triaxial compression test creates a stress–strain relationship under confined conditions, which confirms the strengthening of hydrate-bearing sediment with confining pressure.
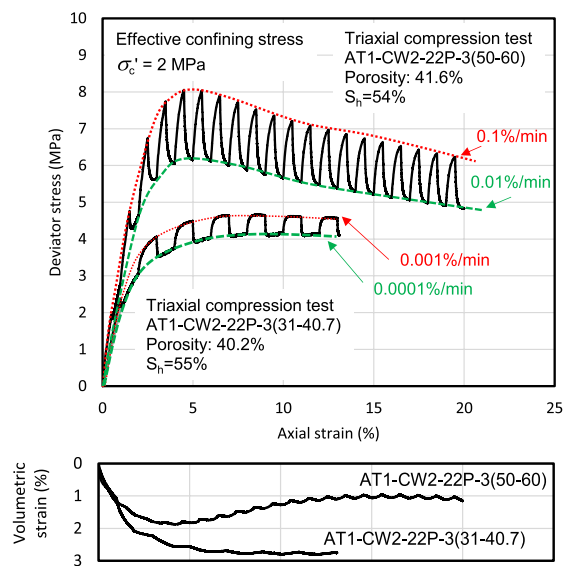

Fig. 6 Alternating strain rate triaxial compression test results. Stress–strain curves for AT1-CW2-22P-3(50–60) and AT1-CW2-22P-3(31–40.7) and volumetric strain versus axial strain are illustrated

Based on these results, the effect of confining pressure on the strength and stiffness of hydrate-bearing sediments is discussed in the next section.

Next, we consider the strain-rate dependence. Previous studies have demonstrated that the dependence of sand on time is small (Miyazaki et al. 2007, Nakashima 2019, Yoneda et al. 2019a). Therefore, the time-dependence of hydrate-bearing sediments is a manifestation of the nature of the hydrate, which carries the load between soil particles during compaction. Ice is also a strain rate-dependent material that exhibits viscous behavior, such as creep, which is attributed to the friction inside the ice. Mechanisms responsible for that friction include proton rearrangement towing to water molecule rotation (Kneser et al. 1955), dislocation motion of water molecules (Perez et al., 1976), ice crystal-grain boundary sliding, and lattice diffusion creep (Poirier 1985). In the case of slow loading, the main cause of friction is a considered to be grain boundary sliding or lattice diffusion creep. Lattice diffusion creep is the deformation caused by the generation and diffusion of micro-voids between crystals at a level smaller than the grain boundaries. Higher strain rates can result in greater strength, as the micro-void is less likely to spread, whereas slower strain rates can result in lower strength owing to the creep phenomenon. Methane hydrate also demonstrates strain rate dependence because of the effects of grain boundary sliding and micro-void diffusion.

4 Discussion

4.1 Strength

Figure 7A and B displays the relationship between strength and strain rate as a double-logarithmic graph. In addition to the compression test results from the six samples from this study, the results from 5 natural and 12 synthetic samples are also shown in the figure. The hydrate-bearing sediments have a greater line slope in any strain region (Fig. 7A) and hydrate-free sediments shows flat slope line (Fig. 7B). In double-logarithmic graphs, previous studies have reported that strength increases linearly with a strain rate (Durham et al. 2003; Miyazaki et al. 2007; Yoneda et al. 2022). Miyazaki et al. (2007) proposed an equation for the relationship between hydrate saturation using this slope as the strain rate dependence parameter m. Subsequently, by adding the strain rate dependence for the case of 100% (massive) hydrate to the comparison, it was revealed that the strain rate dependence of the strength of hydrate-bearing soil involves the hydrate volume fraction and the following equation is proposed (Fig. 8).

$$m = 0.52 n_h, \tag{1}$$

where m represents the strain rate dependence, and n_h is the hydrate volume content (dimensionless), calculated as $n_h = n \times S_h$. The new formulation parameter m, by including the test results of this study, was confirmed to be the same as the previous formula (Yoneda et al. 2022).
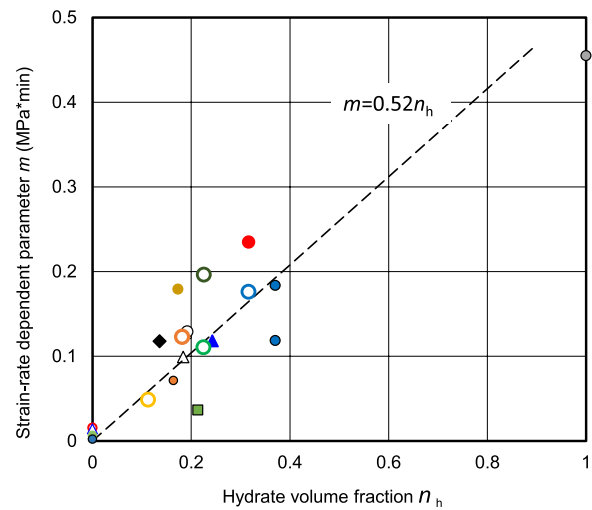

Fig. 8 Strain-rate dependency parameter m vs. hydrate volume fraction

From this, the maximum deviator stress at a given strain rate $R_{\varepsilon a}$ is expressed as:

$$q_{max} = q_{max1} \cdot R_{\varepsilon a}^m, \tag{2}$$

where q_{max} is the maximum deviator stress, q_{max1} is the maximum deviator stress at a strain rate of 1%/min, and $R_\varepsilon a$ is the strain rate in percent per minute. The variable m is expressed as a function of n_h.
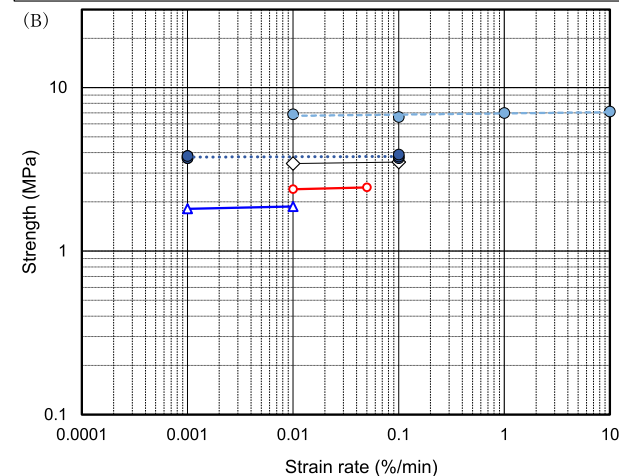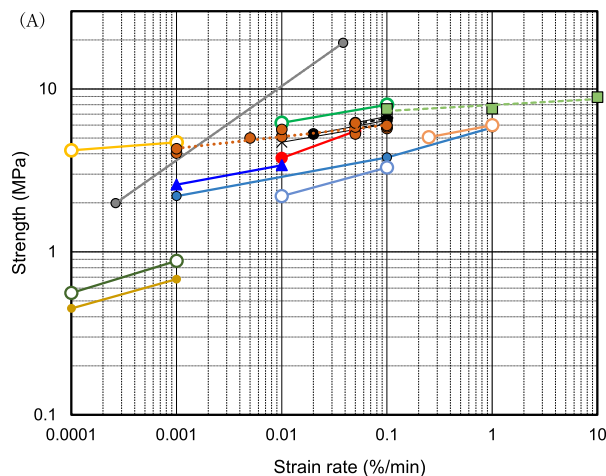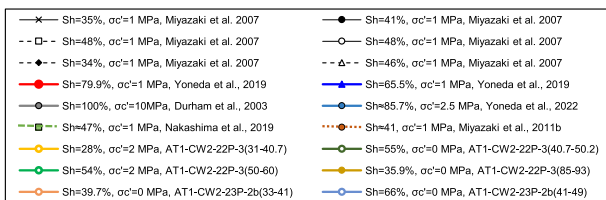

Fig. 7 Strength (maximum deviator stress) versus compression strain rate. **A** Hydrate-bearing sediments. **B** Hydrate free sediments

Figure 9 shows the results of drained triaxial compression tests of synthetic and natural gas hydrate sediments at various previously reported strain rates. They were converted to compressive strength q_{max1} at a strain rate of 1% using Eq. (2) and plotted relative to hydrate saturation. The results are shown for 309 test results, with 80 of the results corresponding to the 53 natural core samples and 229 of the results corresponding to the 223 artificial core samples (see Additional file 1: Data S1). Two major factors may account for the differences between artificial and natural hydrate-bearing sediments. One is the hydrate morphology in the pore spaces of sediments. The other is the physical properties of the host sediments. Regarding hydrate morphology, typical morphologies have been established as cementing type (grain contact and grain coating), pore-filling type, and load-bearing type (matrix supporting) (Waite et al. 2009). The unsaturated system (excess gas method), where methane gas is injected at high pressure into moist sand and temperature controlled to hydrate the meniscus, is recognized for generating cementing-hydrate deposits (Clayton et al. 2005; Priest et al. 2005). Reportedly, when water is passed through gas-saturated methane hydrate sediments, the hydrate morphology changes from cementing type to pore-filling or load-bearing type (Choi et al. 2014). The

triaxial compression strength and deformation modulus of artificial methane hydrate using the excess gas method plus water injection exhibit a strong correlation with the pressure core results (Yoneda et al. 2015a, b). To generate the artificial cores, we decided to include only the drained triaxial compression from the data of the excess gas method plus water injection, which demonstrated a strong correlation with the results of the natural cores. In Fig. 9, for each effective confining pressure, a nonlinear increase in strength occurs with increased hydrate saturation. In previous studies, the mechanical properties of the soils were frequently expressed in terms of the Mohr–Coulomb failure criterion with Terzaghi's effective stress principle ($\tau = c' + \sigma \tan\phi'$), which is utilized in numerical simulations. Here, τ is shear stress, c' is cohesion, σ' is normal stress, and ϕ' is the friction angle of the effective stress. This model can represent changes in strength with increasing effective confining pressure by expressing strength in terms of the apparent cohesion and friction angle. Figure 9 shows that hydrate-bearing sediments with zero effective confining stress exhibit uniaxial compression strength, indicating cohesion owing to the presence of hydrates. In practice, applying a compression test to sediment after hydrate dissociation under unconfined conditions is not possible. The sample could not even
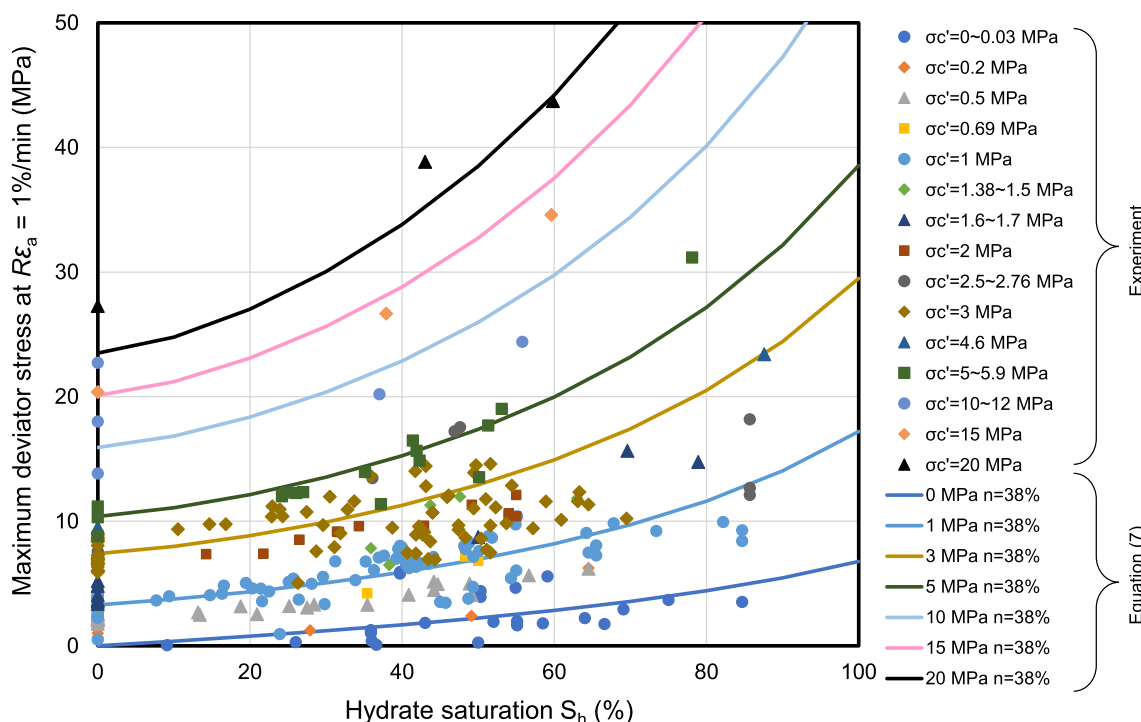

Fig. 9 Normalized strength evolution of previous studies with hydrate saturation at strain rate $R\varepsilon_a = 1\%/min$ (Masui et al. 2005, 2007; Miyazaki et al. 2007, 2011a, b; Yun et al. 2007; Hyodo et al. 2013b, 2017; Yoneda et al. 2015a, b, 2017, 2019a, 2021, 2022; Choi et al. 2018; Nakata et al. 2018; Nakashima 2019; Priest and Hayley 2019; Xu et al. 2022). Plots are categorized by effective confining stress. The solid lines are predicted values based on the proposed Eq. (7)

stand on its own because it is an unconsolidated (coarse) sediment. A uniaxial compressive strength of zero effective confining pressure indicates cohesion owing to the adhesion component at zero normal stress in the Mohr–Coulomb failure criterion. The increase in strength is smaller for smaller effective confining pressures and larger for larger effective confining pressure owing to the increase in the peak friction angle corresponding to the increase in the bulk solid (soil particles and hydrate crystals) density caused by the hydrate. Previous studies have also shown that the angle of the failure shear band increases with hydrate abundance in compression tests under plane strain and triaxial conditions using a thick acrylic observation window and X-ray CT, respectively (Yoneda et al. 2013a, b, 2016; Kajiyama et al. 2017). Therefore, the presence of hydrate increases not only the cohesion but also the internal peak friction angle. Consequently, the following strength estimation equation has been proposed (Yoneda et al. 2017) by modifying the equations of Miyazaki et al. (2007) and Jung and Santamarina (2011), based on the triaxial testing results for a compression strain rate of 0.1%/min, which has been previously proposed based on the Mohr–Coulomb fracture criterion.

$$c' = c'_{sand} + 1.6\sigma_t S_h, \qquad \phi' = \phi'_{sand} + \alpha S_h^{\beta}, \quad (3)$$

where c' is the apparent cohesion, c'_{sand} is the apparent cohesion of the sand, σ_t is the hydrate tensile strength (Jung and Santamarina 2011), ϕ' is the peak effective friction angle, ϕ_{sand} is the peak effective friction angle of the hydrate-free sand, and α and β are fitting parameters that determine the degree of strength increase with increasing hydrate saturation.

Here, the cohesion and peak friction angles of hydrate-free sediments are needed to estimate the strength. However, it is nearly impossible to obtain the cohesion and peak friction angle of hydrate-free sediments directly in the actual field before laboratory testing. Therefore, we estimate the parameters by focusing only on hydrate-free sediments from the experimental results in Fig. 10.

Figure 10 shows the relationship between the strength representing the peak deviator stress under the drained condition and the porosity of the hydrate-free sediments. For comparison under the same effective confining pressure, regression analysis was performed based on the results for 0.5, 1, and 3 MPa effective confining pressure. The maximum strength is related to the porosity (void ratio, relative density) (Bolton 1986, Tatsuoka 1986). These results show that for each effective confining pressure, the porosity decreases and the strength increases. Meanwhile, in dense sand, there is a considerable degree of interlocking between particles, and before shear failure can take place, this interlocking must be overcome in
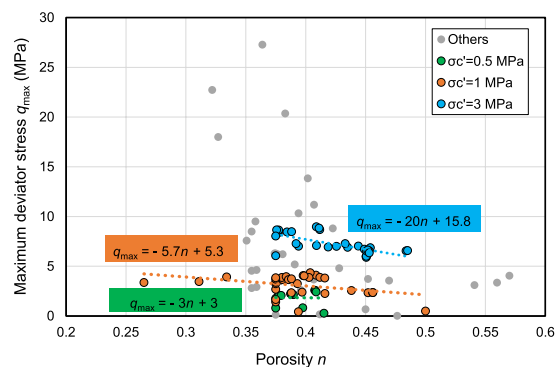

Fig. 10 Maximum deviator stress of hydrate-free sediment vs. porosity

addition to the frictional resistance at the points of contact (Craig 1997). The results for each effective confining stress contain variation, which could be attributed to the differences in the particle size distribution and particle shape. However, this effect was not larger than the effect of the porosity (Additional file 2: Fig. S1). Therefore, the increase in strength (slope of the regression line) at each effective confining pressure is summarized as a linear function of the effective confining pressure. Information on the grain size or shape was not treated as a parameter in the empirical equation, as the equation is currently difficult to determine from the logging and requires coring and a large amount of grain analysis. Consequently, the maximum strength at $S_h = 0$ is expressed by the following equation using the porosity and effective confining pressure,

$$q_{(S_h=0)} = -6.8\sigma_{c'} \cdot n + C, \quad (4)$$

Here, the proportionality constant C is calculated from each test result, such that each plot can be converted to a specific porosity. Figure 11 shows the test results modified to represent 35%, 40%, and 45% porosity.

The strength increases nonlinearly near an effective confining pressure of $\sigma_c' = 3$ MPa. Dense sand has a large peak friction angle at low-confining pressure, decreasing as the confining pressure increases (Bolton 1986, Tatsuoka 1986). Furthermore, the peak friction angle of the dense sand decreases at high confining pressures owing to particle crushing (Bolton 1986, Miura and Yamanouchi, 1977, Vesić and Clough, 1968). Equation (3) presents a linear approximation of this result, showing a component of the apparent cohesion c_{sand}. However, if such a nonlinear increase in strength is linearly modeled to obtain c and ϕ, the low-confining pressure range will be overestimated and the high-pressure range will be underestimated, hindering correct evaluation. Therefore, this study returns to the fact that the cohesive component
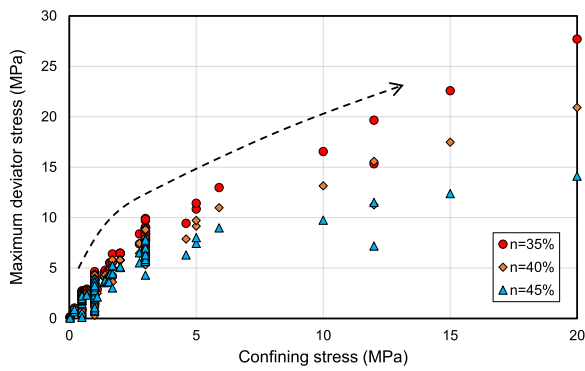
Fig. 11 Strength evolution versus confining stress based on Eq. (4) for different porosities of hydrate-free sediments

of sand is originally zero, and a new evaluation is performed as the secant friction angle of each peak strength. The secant friction angle represents the inclination of a line from the origin to the intersection of a normal stress at failure under Mohr–Coulomb failure criteria. Figure 12 shows the difference between general Mohr–Coulomb failure criteria for dense sand and the secant friction angle for this study. The general Mohr–Coulomb model would produce a cohesion component of the sand. However, with the secant angle, the stress dependency of the failure envelope can be expressed. Figure 13 summarizes the relationship between the secant angle and effective confining pressure at peak strength.
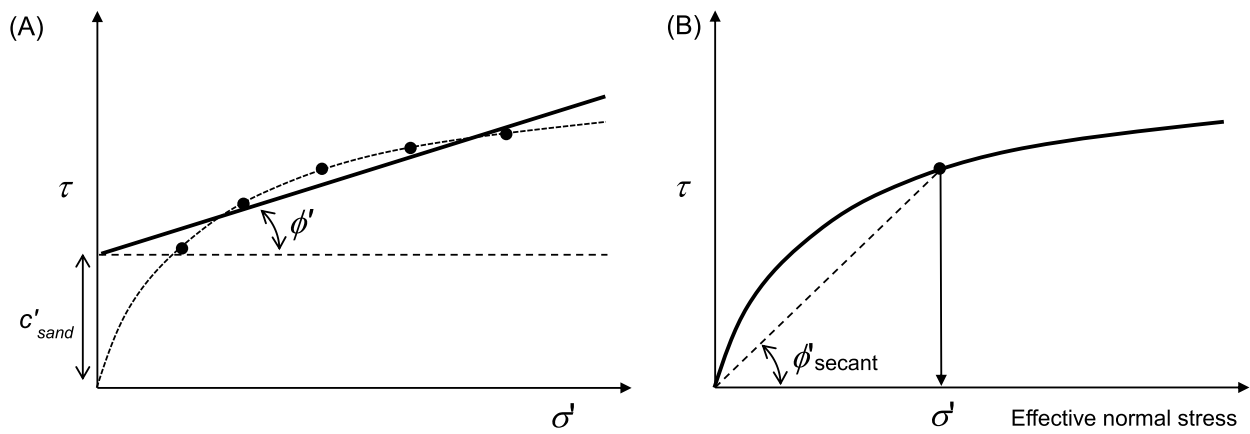
Fig. 12 Models based on Mohr–Coulomb fracture criterion. **A** Effective friction angle and cohesion for dense sand. **B** Secant friction angle
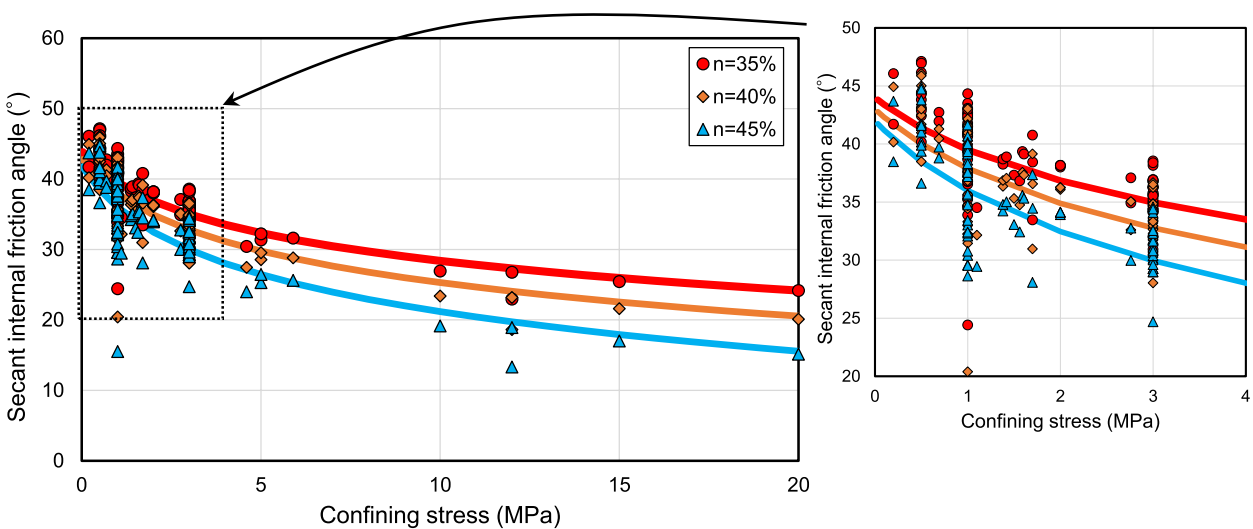

Fig. 13 Secant friction angle of hydrate-free sediments

Equation (5) is obtained to estimate the strength increase, allowing the strength of the hydrate-free sediment to be estimated if the porosity and effective confining pressure are known,

$$\phi_{\text{sand}} = (51 - 20n) + (2.7 - 50n)\log_{10}(1 + \sigma_{c'}) \quad (5)$$

Then, with $c_{\text{sand}} = 0$ from Eq. (3), we propose a new strength estimation equation for hydrate-bearing sediment,

$$c = 1.6\sigma_t S_h, \phi = \phi_{\text{sand}} + \alpha S_h^{\beta} \quad (6)$$

From the relationship between Eq. (6) and the maximum strength ($q_{\max} = \sigma_1 - \sigma_3$ in the Mohr–Coulomb failure criterion), Eq. (7) can be obtained using Eqs. (1), (2), (5), and (6),

$$q_{\max} = \frac{2(\sigma_{c'}\sin\phi + c\cos\phi)}{1 - \sin\phi}R_{\varepsilon_a}^m, \quad (7)$$

where $c = 1.6\sigma_t S_h$, $\sigma_t = 0.5$(MPa), $\phi = \phi_{\text{sand}} + \alpha S_h^{\beta}$, $\phi_{\text{sand}} = (51 - 20n) + (2.7 - 50n)\log_{10}(1 + \sigma_{c'})$, $\alpha = 20$, $\beta = 1.5$, and $m = 0.52n_h = 0.52nS_h$. α, β, and σ_t were determined by multiple regression analysis to have the highest correlation. σ_t is the tensile strength of methane hydrate. In Jung and Santamarina (2011), the direct measurement for the maximum strength was approximately 0.2 MPa: meanwhile, a previous study (Yoneda et al. 2017) also adopted 0.2 MPa. However, Yoneda et al. 2019c and Kida et al. 2021 reported that the strength varies with hydrate crystal grain size. Here we treated σ_t as a fitting parameter. The tensile strength of the hydrate estimated from this regression analysis was 0.5 MPa. Figure 9 overlays the proposed empirical formula. As an example, the predicted values are shown for a porosity of 38% and effective confining pressures of 0, 1, 3, 5, and 10 MPa. Although the experimental values are not directly comparable because of the varying porosity, the increase in strength with increasing hydrate saturation is well represented for each effective confining pressure. Figure 14 shows a cross plot of the predictions calculated using the porosity, strain rate, effective confining pressure, and hydrate saturation for all tests versus the experimental data. The coefficient of determination for all results is 0.95, permitting the estimation of the maximum strength using only the parameters available from the logging data (bulk density, porosity, and hydrate saturation).

4.2 Deformation modulus
Figure 15 shows the deformation modulus and strain rate relationship as previously conducted for strength in Fig. 7. The deformation (/secant/elastic) modulus E_{50} is defined as $E_{50} = (q_{\max}/2)/\varepsilon_{50}$, where, ε_{50} is the axial strain at half the maximum deviator stress. E_{50} is
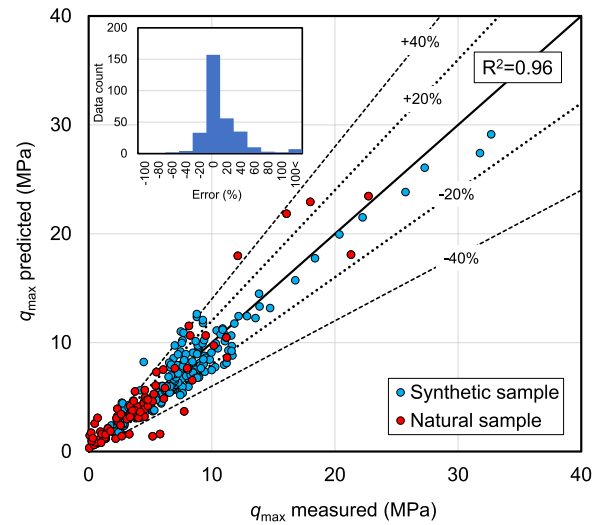

Fig. 14 Predicted and measured maximum deviator stress for synthetic and natural core samples
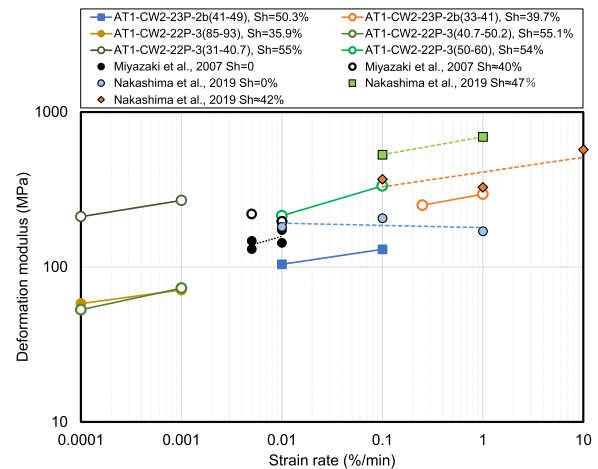

Fig. 15 Strain-rate dependency on the deformation modulus

defined in the standard (JIS A 1216 Method for unconfined compression test of soils, Eurocode 7, 5.9.3 Triaxial deformability testing) and is routinely used for elastic model analysis. The figure shows the results for different hydrate saturations and effective confining pressures. As the strain rate increases, the deformation modulus also increases. Figure 16 shows the parameter m', demonstrating the slope of the deformation modulus in the double-logarithmic graph of Fig. 15. Here, the result for the hydrate free sediment is assumed to have no strain rate dependence, and when approximated by a line passing through the origin, the deformation modulus is shown to be proportional to the hydrate volume fraction, as expressed by $m' = 0.53n_h$.
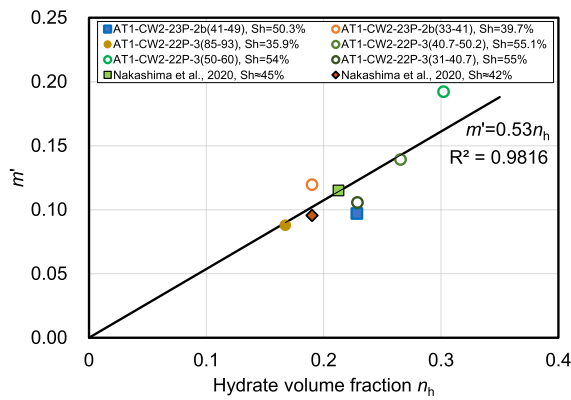
Fig. 16 Strain-rate dependency parameter m vs. hydrate volume fraction for the deformation modulus

Similar to Eq. (2) proposed for strength, the deformation modulus for any given strain rate, based on the deformation modulus at 1% strain rate, is expressed by Eq. (8),

$$E_{50} = E_{501} R_{\varepsilon_a}^{m'}. \tag{8}$$

Using Eq. (8), all results are converted to the $R_{\varepsilon a} = 1\%$ strain rate case (Fig. 17). Although the data varied widely, the deformation modulus shows a log-linear relationship with the hydrate saturation.

The rate of increase is constant even when the effective confining pressure is changed. Therefore, the deformation coefficient is expressed as the product of a function of the effective confining pressure and porosity, the exponential function of the hydrate saturation rate, and the strain rate,

$$E_{50} = f(\sigma_{c'}, n) \cdot \exp(aS_h) R_{\varepsilon_a}^{m'}, \tag{9}$$

Then, the deformation modulus for hydrate-free sediment is expressed as:

$$E_{50} = f(\sigma_{c'}, n) \cdot R_{\varepsilon_a}^{m}. \tag{10}$$

Figure 18 shows the relationship between the deformation modulus and effective confining pressure of the sediment without hydrate. The figure plots are colored differently for each porosity. Although there is some variation owing to the different porosity and difference grain size, the deformation modulus increases nearlinearly with increasing effective confining pressure. The effect of the grain size is shown in Additional file 2: Fig. S2. A large difference is seen in the results for the effective confining pressure of 12 MPa; here, the higher confining pressure results in a strain-hardening type stress–strain relationship, producing in a smaller deformation modulus. In addition, particle crushing might be another factor.
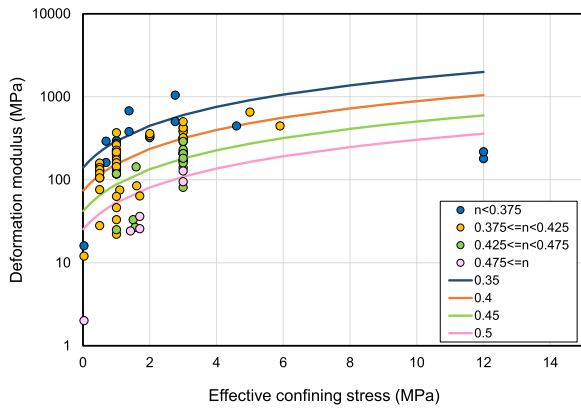

Fig. 17 Deformation modulus vs. hydrate saturation under various effective confining stresses (Yun et al. 2007, Miyazaki et al. 2011a, b; Hyodo et al. 2013b; Yoneda et al. 2015a, 2015b, 2019a, b, c, 2021; Choi et al. 2018; Nakashima 2019)

Fig. 18 Deformation modulus versus effective confining stress for hydrate-free sediments

Figure 19 shows the relationship between the deformation modulus and porosity. Larger porosity corresponds with lower strength, while smaller porosity corresponds with higher strength. An approximation of the magnitude of the power is used to estimate the deformation coefficient of the porosity.

Therefore, the parameters with the highest coefficients of determination were obtained by multiple regression analysis, under the assumption that the coefficient of deformation for hydrate-free sediments can be derived from the following relationship,

$$E_{50\_\text{sand}} = (a\sigma_{c'} + b) \cdot n^c. \tag{11}$$

The results show that $a=1$, $b=0.9$, and $c=-4.8$, with the coefficient of determination$=0.65$.

Empirical Eq. (11) is substituted into Eq. (9) to obtain the parameter α that is most correlated to the hydrate saturation. The result was $\alpha=1.7$, and the estimated equation for the deformation modulus is obtained as
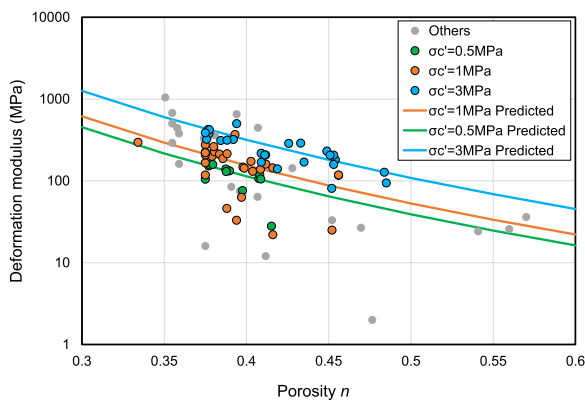
$$E_{50} = (\sigma_{c'} + 0.9)n^{-4.8}\exp(1.7S_h)R_{\varepsilon_a}^{0.53nS_h}. \tag{12}$$

Figure 17 shows the results predicted by Eq. (12) as solid lines. Figure 20 shows a cross plot of the predicted and measured values for all the test results. Although the correlation coefficient is 0.24 and some variation is observed, the deformation modulus could be estimated for hydrate-bearing sediments. The results for the synthetic samples correlate well, but the natural core samples are scattered. Studies have been reported on the differences in the physical properties of host sediments, with an emphasis on grain size distribution and clay content (Hyodo et al. 2017; Priest and Hayley 2019). These differences, this may be due to the fact that it is very difficult to form the end faces with pressure core technology, and it is extremely difficult to make the top and bottom faces of the specimen parallel. Furthermore, natural cores can be heterogeneous, and it is presumed that the stiffness, which is more sensitive than the strength, has varied (Additional file 3).

More than a dozen simulators have been proposed to predict seabed ground deformation during methane hydrate production, and advanced numerical simulations such as elasto-plastic and elasto-visco-plastic analyses are available based on elastic analysis (White et al. 2020). Most simulators use multiple time steps separated by a short period to solve for kinetic hydrate dissociation. In using the above equations, the strain rate of a previous time step can be applied. In this case, the deformation is overestimated in the increased strain rate step and underestimated in the decreased strain rate step. Therefore, the analysis step should be as small as possible. We
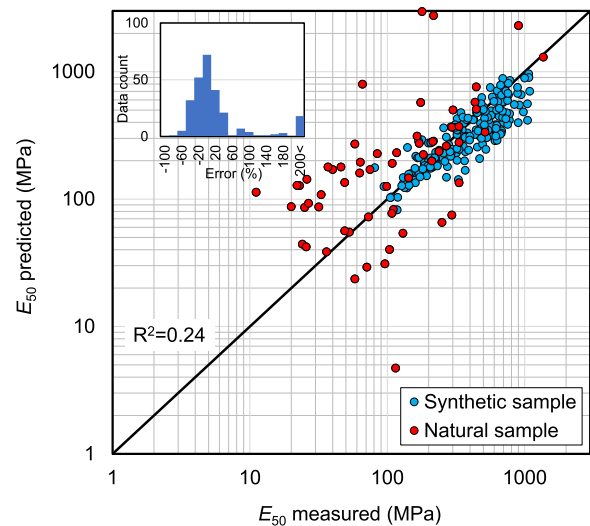

Fig. 19 Deformation modulus versus porosity for hydrate-free sediments

Fig. 20 Predicted and measured deformation modulus for hydrate-bearing and hydrate-free sediments

believe that the ultimate results will have much less error than an analysis that does not consider the strain rate.

The equations proposed in this study empirically predict the deformation modulus E_{50} and the peak strength. Therefore, residual strength and dilatancy properties after failure are not considered. In cases in which the formation is subjected to large deformation, stress–strain relationships and dilatancy properties must be evaluated using a constitutive model based on the critical state soil mechanics, such as the constitutive model for hydrate-bearing sediments, which is based on the Cam–Clay model (Uchida et al. 2012).

Finally, Fig. 21 shows the depth profiles of the strength and deformation modulus calculated using Eqs. (7) and (12) from the AT1-CW2 porosity, bulk density, P- and S-wave velocities, and hydrate saturation obtained from logging. The vertical effective stress σ_{v}' is the sum of the bulk density from the seafloor. The confining pressure was assumed to be the mean effective stress. Here, $\sigma_{c}' = \sigma_{v}' + 2K_0\sigma_{v}'$. The coefficient of earth pressure at rest (K_0) was calculated using Poisson's ratio ($v = (1/2 (V_p/V_s)^2 - 1)/((V_p/V_s)^2 - 1)$) calculated from the P- and S-wave velocities; in elastic ratio, Poisson's ratio and $K_0 = v/(1-v)$ are related. If the P- and S-wave velocities are not measured in the reservoir, the equation $K_0 = 1 - \sin\phi'$ can be used (Jaky 1944, 1948). Furthermore,

the dynamic elastic modulus calculated from V_p using the relation $E = \rho V_p^2 (1+v)(1-2v)/(1-v)$ is also shown in the figure for reference. The deformation (elastic) modulus of the core sample was approximately 1/10 of the dynamic elastic modulus from the previous study (Yoneda et al. 2021). The deformation modulus becomes smaller than the dynamic modulus, as it is the secant modulus for the average stiffness before the peak strength. In addition, the dynamic modulus is measured by sonic waves that pass through the fastest zone, indicating waves through the stiffest zone. Meanwhile, the specimen starts to deform from the weakest zone. The figure shows the core test results obtained in this study, modified as strength at a strain rate of 1%. It is confirmed that the proposed equation provides good prediction results for the deformation modulus and strength.

5 Conclusions

Samples were recovered by pressure coring to clarify the strength and deformation characteristics of methane hydrate-bearing sediments from the same site in the Nankai Trough, where the second offshore gas production test was performed, and triaxial and uniaxial compression tests under different strain rates were conducted. The compression test results at an unprecedentedly slow strain rate of 0.0001%/min revealed
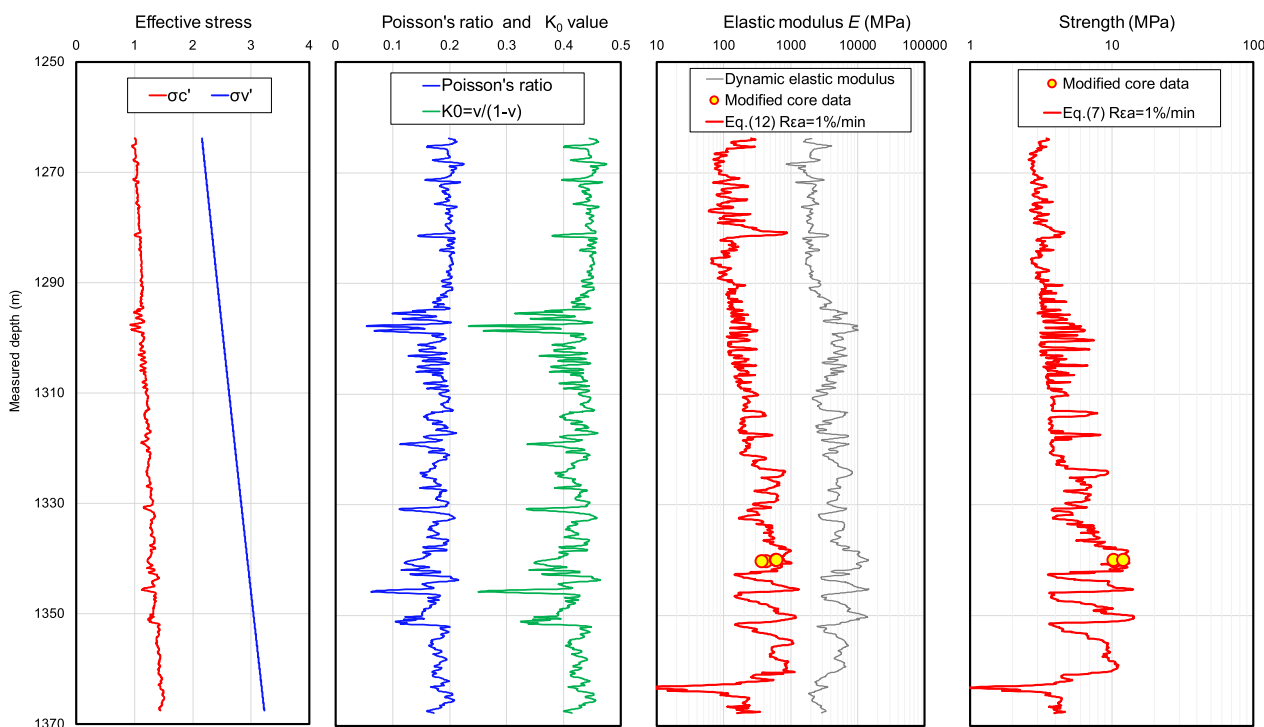

Fig. 21 Strength and deformation modulus prediction based on the proposed empirical equation and logging data. Hydrate saturation in Eqs. (7) and (12) were based on the prediction by Archie's equation

Yoneda *et al. Progress in Earth and Planetary Science* (2024) 11:3

Page 16 of 18

that the increase in strength owing to the presence of hydrate was slight. However, the compressive strength at a strain rate of 1%/min was approximately ten times greater than the result for 0.0001%/min. In this case, the strain rate dependence is expressed in a log-linear fashion, as in previous studies. Based on an evaluation of the strength and deformation parameters obtained and the results of previous core tests, the empirical Eqs. (7) for strength and (12) for the deformation modulus were proposed, allowing the prediction of the in situ compressive strength and deformation modulus by setting the parameters obtained from the log: porosity, bulk density for calculating the effective stress, hydrate saturation, and strain rate corresponding to an assumed strain rate. These predictions do not include the effect of particle size and shape and may contain errors of $\pm 40\%$. Note that caution should be exercised in practical use. This study allows predictions of the strength and stiffness based on the parameters obtained from the well-log. However, reference measurements from coring and laboratory tests are required to yield more accurate reservoir parameters. Finally, Eqs. (7) and (12) are reiterated and described.

Empirical Eq. (7) for the strength (maximum deviator stress) of hydrate-bearing sediment.

$$q_{\max} = \frac{2(\sigma_{c'}\sin\phi + c\cos\phi)}{1 - \sin\phi} R_{\varepsilon_a}^m,$$

where $\sigma_{c'} =$ effective confining stress (MPa), $c = 1.6\sigma_\mathrm{t}S_\mathrm{h}$, $\sigma_\mathrm{t} = 0.5\,(\mathrm{MPa})$, $\phi = \phi_\mathrm{sand} + \alpha S_\mathrm{h}^{\beta}$, $\phi_\mathrm{sand} = (51 - 20n) + (2.7 - 50n)\log_{10}(1 + \sigma_{c'})$, $\alpha = 20, \beta = 1.5$, and $m = 0.52nS_\mathrm{h}, R_{\varepsilon_a} =$ strain rate (%/min), $n =$ porosity, and $S_\mathrm{h} =$ hydrate saturation.

Empirical Eq. (12) for the stiffness (deformation modulus) of hydrate-bearing sediment.

$$E_{50} = (\sigma_{c'} + 0.9)n^{-4.8}\exp(1.7S_h)R_{\varepsilon_a}^{m'}$$

where $m' = 0.53nS_\mathrm{h}$.

Abbreviations

AIST	Advanced Industrial Science and Technology
CT	Computed tomography
JOGMEC	Japan Oil, Gas and Metals National Corporation
PNAT	Pressure core Nondestructive Analysis Tools
TACTT	Transparent acrylic cell triaxial testing
THF	Tetrahydrofuran

Supplementary Information

The online version contains supplementary material available at https://doi.org/10.1186/s40645-024-00606-1.

Additional file 1. Data summary table of triaxial test results for gas hydrate-bearing sediments.

Additional file 2. Effect of grain size (Median) on the maximum deviator stress and deformation modulus under triaxial compression of gas hydrate-bearing sediments.

Additional file 3. Borehole physical property data sheet for AT1-CW2.

References

Bolton MD (1986) The strength and dilatancy of sands. Géotechnique 36:65–78. https://doi.org/10.1680/geot.1986.36.1.65

Choi J-H, Dai S, Cha J-H, Seol Y (2014) Laboratory formation of noncementing hydrates in sandy sediments. Geochem Geophys Geosyst 15:1648–1656. https://doi.org/10.1002/2014GC005287

Choi J-H, Dai S, Lin J-S, Seol Y (2018) Multistage triaxial tests on laboratory-formed methane hydrate bearing sediments. J Geophys Res Solid Earth 123:3347–3357. https://doi.org/10.1029/2018JB015525

Clayton CRI, Priest JA, Best AI (2005) The effects of disseminated methane hydrate on the dynamic stiffness and damping of a sand. Geotechnique 55:423–434. https://doi.org/10.1680/geot.2005.55.6.423

Collett TS, Boswell R, Waite WF, Kumar P, Roy SK, Chopra K, Singh SK, Yamada Y, Tenma N, Pohlman J, Zyrianova M (2019) India National Gas Hydrate Program Expedition 02 summary of scientific results: gas hydrate systems along the eastern continental margin of India. Mar Petrol Geol 108:39–142. https://doi.org/10.1016/j.marpetgeo.2019.05.023

Craig RF (1997) Soil Mechanics, 6th edn. Spon Press is an imprint of the Taylor & Francis Group, London0

Durham WB, Kirby SH, Stern LA, Zhang W (2003) The strength and rheology of methane clathrate hydrate. J Geophys Res 108:2182. https://doi.org/10.1029/2002JB001872

Egawa K, Nishimura O, Izumi S, Fukami E, Jin Y, Kida M, Konno Y, Yoneda J, Ito T, Suzuki K, Nakatsuka Y, Nagao J (2015) Bulk sediment mineralogy of gas hydrate reservoir at the East Nankai offshore production test site. Mar Petrol Geol 66:379–387. https://doi.org/10.1016/j.marpetgeo.2015.02.039

Elger J, Berndt C, Rüpke L, Krastel S, Gross F, Geissler WH (2018) Submarine slope failures due to pipe structure formation. Nat Commun 9:715. https://doi.org/10.1038/s41467-018-03176

Fang Y, Flemings PB, Germaine JT, Daigle H, Phillips SC, O'Connell J (2021) Compression behavior of hydrate-bearing sediments. AAPG Bull 106(5):1101–1126. https://doi.org/10.1306/01132221002

Flemings PB, Phillips SC, Boswell R, Collett TS, Cook AE, Dong T, Frye M, Goldberg DS, Guerin G, Holland ME, Jang J, Meazell K, Morrison J, O'Connell JI, Petrou EG, Pettigrew T, Polito PJ, Portnov A, Santra M, Schultheiss PJ, Seol Y, Shedd W, Solomon EA, Thomas CM, Waite WF, You K (2020) Pressure coring a Gulf of Mexico deep-water turbidite gas hydrate reservoir: initial results from the University of Texas-Gulf of Mexico 2–1 (UT-GOM2-1) hydrate pressure coring expedition. AAPG Bull 104:1847–1876. https://doi.org/10.1306/05212019052

Hyodo M, Nakata Y, Yoshimoto N, Ebinuma T (2005) Basic research on the mechanical behavior of methane hydrate-sediments mixture. Soils Found 45:78–85. https://doi.org/10.3208/sandf.45.1_75

Hyodo M, Li Y, Yoneda J, Nakata Y, Yoshimoto N, Nishimura A, Song Y (2013a) Mechanical behaviorof gas-saturated methane hydrate-bearing sediments. J Geophys Res Solid Earth 118:5185–5194. https://doi.org/10.1002/2013JB010233

Hyodo M, Yoneda J, Yoshimoto N, Nakata Y (2013b) Mechanical and dissociation properties of methane hydrate-bearing sand in deep seabed. Soils Found 53:299–314. https://doi.org/10.1016/j.sandf.2013.02.010

Hyodo M, Wu Y, Nakashima K, Kajiyama S, Nakata Y (2017) Influence of fines content on the mechanical behavior of methane hydrate-bearing sediments. J Geophys Res Solid Earth 122:7511–7524. https://doi.org/10.1002/2017JB014154

Ito T, Komatsu Y, Fujii T, Suzuki K, Egawa K, Nakatsuka Y, Konno Y, Yoneda J, Jin Y, Kida M, Nagao J, Minagawa H (2015) Lithological features of hydrate-bearing sediments and their relationship with gas hydrate saturation in the eastern Nankai Trough, Japan. Mar Petrol Geol 66:368–378. https://doi.org/10.1016/j.marpetgeo.2015.02.022

Jaky J (1944) The coefficient of earth pressure at rest. In Hungarian. J Soc Hung Architects Eng 355–358

Jaky J (1948) Pressure in silos. In: Proceedings of the 2nd international conference on soil mechanics and foundation engineering 1:103–107

Jin Y, Konno Y, Yoneda J, Kida M, Nagao J (2016) In situ methane hydrate Morphology Investigation: Natural Gas hydrate-bearing Sediment Recovered from the Eastern Nankai Trough Area. Energy Fuels 30:5547–5554. https://doi.org/10.1021/acs.energyfuels.6b00762

Jung JW, Santamarina JC (2011) Hydrate adhesive and tensile strengths. Geochem Geophys Geosyst. https://doi.org/10.1029/2010GC003495

Kajiyama S, Hyodo M, Nakata Y, Yoshimoto N, Wu Y, Kato A (2017) Shear behaviour of methane hydrate bearing sand with various particle characteristics and fines. Soils Found 57:176–193. https://doi.org/10.1016/j.sandf.2017.03.002

Kida M, Yoneda J, Masui A, Konno Y, Jin Y, Nagao J (2021) Mechanical properties of polycrystalline tetrahydrofuran hydrates as analogs for massive natural gas hydrates. J Nat Gas Sci Eng 96:104284. https://doi.org/10.1016/j.jngse.2021.104284

Kimoto S, Oka F, Fushita T (2010) A chemo-thermo-mechanically coupled analysis of ground deformation induced by gas hydrate dissociation. Int J Mech Sci 52:365–376. https://doi.org/10.1016/j.ijmecsci.2009.10.008

Klar A, Uchida S, Soga K, Yamamoto K (2013) Explicitly coupled thermal-flow-mechanical formulation for gas hydrate sediments. SPE J 18:196–206. https://doi.org/10.2118/162859-PA

Kneser HO, Magun S, Ziegler G (1955) Mechanischen Relaxation von einkristallinen eis. Naturwissenschaften 42:437. https://doi.org/10.1007/BF00599816

Kurihara M, Sato A, Ouchi H, Narita H, Masuda Y, Saeki T, Fujii T (2008) Prediction of gas productivity from eastern Nankai Trough methane hydrate reservoirs. In: All Days, OTC, Offshore Technology Conference, Houston, Texas, 5–8 May, 2008 19382. https://doi.org/10.4043/19382-MS.

Masui A, Haneda H, Ogata Y, Aoki K (2005) The effect of saturation degree of methane hydrate on the shear strength of synthetic methane hydrate sediments. In: The Fifteenth International Offshore and Polar Engineering Conference, 19–24 June, Seoul, Korea, Paper ref 2037. 657–663.

Masui A, Haneda H, Ogata Y, Aoki K (2007). Mechanical properties of sandy sediment containing marine gas hydrates in deep sea offshore Japan.

In: Proceedings of the 7th ISOPE-OMS, Lisbon, International Society of Offshore and Polar Engineers, USA. 53–56.

Miura N, Yamanouchi T (1977) Effect of particle-crushing on the shear characteristics of a sand. Proceed Japan Soc Civil Eng 260:109–118. https://doi.org/10.2208/jscej1969.1977.260_109

Miyazaki K, Masui A, Sakamoto Y, Haneda H, Ogata Y, Aoki K, Yamaguchi T, Okubo S (2007) Strain rate dependency of sediment containing synthetic methane hydrate in triaxial compression test. J MMIJ 123:537–544. https://doi.org/10.2473/journalofmmij.123.537

Miyazaki K, Yamaguchi T, Sakamoto Y, Tenma N, Ogata Y, Aoki K (2010) Effect of confining pressure on mechanical properties of sediment containing synthetic methane hydrate. J MMIJ 126:408–417. https://doi.org/10.2473/journalofmmij.126.408

Miyazaki K, Masui A, Sakamoto Y, Aoki K, Tenma N, Yamaguchi T (2011a) Triaxial compressive properties of artificial methane-hydrate-bearing sediment. J Geophys Res 116:B06102. https://doi.org/10.1029/2010JB008049

Miyazaki K, Yamaguchi T, Sakamoto Y, Aoki K (2011b) Time-dependent behaviors of methane-hydrate bearing sediments in triaxial compression test. Int J JCRM. 7:43–48. https://doi.org/10.11187/ijjcrm.7.43

Nagao J (2012) Development of methane hydrate production method. Synthesiology 5:89–97. https://doi.org/10.5571/synth.5.89

Nakashima K (2019) Mechanical characteristics and elasto-viscoplastic constitutive model for methane hydrate-bearing sediments in Eastern Nankai Trough, p151. Yamaguchi University, Japan 2019:3

Nakata Y, Kajiyama S, Hyodo M, Yoshimoto N, Hiraoka S, Nakashima K, Shimamoto R (2018) Creep behavior of methane hydrate bearing sand under triaxial compression loading. In: Proceedings of the IS-Atlanta 2018 Geo-Mechanics from Micro to Macro in Research & Practice, ISA-099_11, 10–12 Sep., Atlanta.

Nishioka I, Nakatsuka Y, Yamamoto K (2018) Pressure coring operation at the eastern Nankai Trough after the second offshore gas production test, American Geophysical Union, Fall Meeting 2018, #OS23D-1652, 10–14 Dec 2018, Washington, D.C.

Ouchi H, Yamamoto K, Akamine K, Kano S, Naiki M, Tamaki M, Ohtsuki S, Kanno T, Tenma N (2022) Numerical history-matching of modeling and actual gas production behavior and causes of the discrepancy of the Nankai Trough gas-hydrate production test cases. Energy Fuels 36:210–226. https://doi.org/10.1021/acs.energyfuels.1c02931

Paull CK, Ussler W, Holbrook WS (2007) Assessing methane release from the colossal Storegga submarine landslide. Geophys Res Lett 34:L04601. https://doi.org/10.1029/2006GL028331

Perez J, Mai C, Tatibouet J, Cassoille R (1976) Internal friction and microplasticity of ice I$_h$. Nuovo Cimento 33b:86–95. https://doi.org/10.1007/BF02722474

Poirier JP (1985) Creep of crystals. Oxford University Press, Oxford. https://doi.org/10.1017/CBO9780511564451

Priest JA, Hayley JL (2019) Strength of laboratory synthesized hydrate-bearing sands and their relationship to natural hydrate-bearing sediments. J Geophys Res Solid Earth 124:12556–12575. https://doi.org/10.1029/2019JB018324

Priest JA, Best AI, Clayton CRI (2005) A laboratory investigation into the seismic velocities of methane gas hydrate-bearing sand. J Geophys Res 110:B04102. https://doi.org/10.1029/2004JB003259

Priest JA, Druce M, Roberts J, Schultheiss P, Nakatsuka Y, Suzuki K (2015) PCATS Triaxial: a new geotechnical apparatus for characterizing pressure cores from the Nankai Trough, Japan. Mar Petrol Geol 66:460e470. https://doi.org/10.1016/j.marpetgeo.2014.12.005

Rutqvist J, Moridis GJ, Grover T, Collett T (2009) Geomechanical response of permafrost-associated hydrate deposits to depressurization-induced gas production. J Petrol Sci Eng 67:1–12. https://doi.org/10.1016/j.petrol.2009.02.013

Schultheiss PJ, Francis TJG, Holland M, Roberts JA, Amann H, Parkes TRJ et al (2006) Pressure coring, logging and subsampling with the HYACINTH system. SP Publ 267:151–163. https://doi.org/10.1144/GSL.SP.2006.267.01.11

Shin H, Santamarina JC (2016) Sediment-well interaction during depressurization. Acta Geotech 12:883–895. https://doi.org/10.1007/s11440-016-0493-1

Sloan ED Jr (2003) Fundamental principles and applications of natural gas hydrates. Nature 426:353–363. https://doi.org/10.1038/nature02135

Tatsuoka F, Sakamoto M, Kawamura T, Fukushima S (1986) Strength and deformation characteristics of sand in plane strain compression at extremely

low pressures. Soils Found 26:65–84. https://doi.org/10.3208/sandf1972.26.65

Uchida S, Soga K, Yamamoto K (2012) Critical state soil constitutive model for methane hydrate soil. J Geophys Res 117:1–13. https://doi.org/10.1029/2011JB008661

Vesić AS, Clough GW (1968) Behavior of granular materials under high stresses. J Soil Mech Found Div 94(3): 661–688. https://doi.org/10.1061/JSFEAQ.000113

Waite WF, Santamarina JC, Cortes DD, Dugan B, Espinoza DN, Germaine J, Jang J, Jung JW, Kneafsey TJ, Shin H, Soga K, Winters WJ, Yun T-S (2009) Physical properties of hydrate-bearing sediments. Rev Geophys 47:RG4003. https://doi.org/10.1029/2008RG000279

White MD, Kneafsey TJ, Seol Y, Waite WF, Uchida S, Lin JS, Myshakin EM, Gai X, Gupta S, Reagan MT, Queiruga AF, Kimoto S, Baker RC, Boswell R, Ciferno J, Collett T, Choi J, Dai S, De La Fuente M, Fu P, Fujii T, Intihar CG, Jang J, Ju X, Kang J, Kim JH, Kim JT, Kim SJ, Koh C, Konno Y, Kumagai K, Lee JY, Lee WS, Lei L, Liu F, Luo H, Moridis GJ, Morris J, Nole M, Otsuki S, Sanchez M, Shang S, Shin C, Shin HS, Soga K, Sun X, Suzuki S, Tenma N, Xu T, Yamamoto K, Yoneda J, Yonkofski CM, Yoon HC, You K, Yuan Y, Zerpa L, Zyrianova M, IGHCCS2 Participants (2020) An international code comparison study on coupled thermal, hydrologic and geomechanical processes of natural gas hydrate-bearing sediments. Mar Petrol Geol 120:104566. https://doi.org/10.1016/j.marpetgeo.2020.104566

Xu J, Xu C, Yoshimoto N, Hyodo M, Kajiyama S, Huang L (2022) Experimental investigation of the mechanical properties of methane hydrate–bearing sediments under high effective confining pressure. J Geotech Geoenviron Eng 148:04021190. https://doi.org/10.1061/(ASCE)GT.1943-5606.0002728

Yamamoto K (2015) Overview and introduction: Pressure core-sampling and analyses in the 2012–2013 MH21 offshore test of gas production from methane hydrates in the eastern Nankai Trough. Mar Petrol Geol 66:296–309. https://doi.org/10.1016/j.marpetgeo.2015.02.024

Yamamoto K, Nagakubo S (2021) Review of energy efficiency of the gas production technologies from gas hydrate-bearing sediments. Front Energy Res 9:741715. https://doi.org/10.3389/fenrg.2021.741715

Yamamoto K, Kanno T, Ouchi H, Akamine K, Kano S, Naiki M, Tamaki M, Ohtsuki S, Tenma N (2021) Comparison of the vertical gas-hydrate production profile with the simulation results obtained using geophysical log-based reservoir characteristics and reasons for their discrepancies in the Nankai Trough. Energy Fuels 35:20026–20036. https://doi.org/10.1021/acs.energyfuels.1c02930

Yamamoto K, Suzuki K, Wang X, Matsunaga T, Nishioka I, Nakatsuka Y, Yoneda J (2019). The second offshore production test of methane hydrates in the Eastern Nankai Trough and site characterization efforts, Fire in the ice, A newsletter published by the U.S. Department of Energy's National Energy Technology Laboratory 19:9–15.

Yoneda J, Masui A, Tenma N, Nagao J (2013a) Triaxial testing system for pressure core analysis using image processing technique. Rev Sci Instrum 84:114503. https://doi.org/10.1063/1.4831799

Yoneda J, Hyodo M, Yoshimoto N, Nakata Y, Kato A (2013b) Development of high-pressure low-temperature plane strain testing apparatus for methane hydrate-bearing sand. Soils Found 53:774–783. https://doi.org/10.1016/j.sandf.2013.08.014

Yoneda J, Masui A, Konno Y, Jin Y, Egawa K, Kida M, Ito T, Nagao J, Tenma N (2015a) Mechanical behavior of hydrate-bearing pressure core sediments visualized under tri-axial compression. Mar Petrol Geol 66:451–459. https://doi.org/10.1016/j.marpetgeo.2015.02.028

Yoneda J, Masui A, Konno Y, Jin Y, Egawa K, Kida M, Ito T, Nagao J, Tenma N (2015b) Mechanical properties of hydrate-bearing turbidite reservoir in the first gas production test site of the Eastern Nankai Trough. Mar Petrol Geol 66:471–486. https://doi.org/10.1016/j.marpetgeo.2015.02.029

Yoneda J, Jin Y, Katagiri J, Tenma N (2016) Strengthening mechanism of cemented hydrate-bearing sand at microscales. Geophys Res Lett 43:7442–7450. https://doi.org/10.1002/2016GL069951

Yoneda J, Masui A, Konno Y, Jin Y, Kida M, Katagiri J, Nagao J, Tenma N (2017) Pressure-core-based reservoir characterization for geomechanics: Insights from gas hydrate drilling during 2012–2013 at the eastern Nankai Trough. Mar Petrol Geol 86:1–16. https://doi.org/10.1016/j.marpetgeo.2017.05.024

Yoneda J, Takiguchi A, Ishibashi T, Yasui A, Mori J, Kakumoto M, Aoki K, Tenma N (2018) Mechanical response of reservoir and well completion of the first offshore methane-hydrate production test at the Eastern Nankai Trough: a coupled thermos-hydromechanical Analysis. SPE J SPE. 19:1145

Yoneda J, Oshima M, Kida M, Kato A, Konno Y, Jin Y, Jang J, Waite WF, Kumar P, Tenma N (2019a) Pressure core based onshore analysis on mechanical properties of hydrate-bearing sediments recovered during India's National Gas Hydrate Program Expedition NGHP-02. Mar Petrol Geol 108:482–501. https://doi.org/10.1016/j.marpetgeo.2018.09.005

Yoneda J, Oshima M, Kida M, Kato A, Konno Y, Jin Y, Tenma N (2019b) Consolidation and hardening behavior of hydrate-bearing pressure-core sediments recovered from the Krishna-Godavari Basin, offshore India. Mar Petrol Geol 108:512–523. https://doi.org/10.1016/j.marpetgeo.2018.09.021

Yoneda J, Kida M, Konno Y, Jin Y, Morita S, Tenma N (2019c) In situ mechanical properties of shallow gas hydrate deposits in the deep seabed. Geophys Res Lett 46:14459–14468. https://doi.org/10.1029/2019GL084668

Yoneda J, Jin Y, Muraoka M, Oshima M, Suzuki K, Walker M, Otsuki S, Kumagai K, Collett TS, Boswell R, Okinaka N (2021) Multiple physical properties of gas hydrate-bearing sediments recovered from Alaska North Slope 2018 Hydrate-01 Stratigraphic Test Well. Mar Petrol Geol 123:104748. https://doi.org/10.1016/j.marpetgeo.2020.104748

Yoneda J, Jin Y, Muraoka M, Oshima K, Suzuki WF, Waite FPB (2022) Comprehensive pressure core analysis for hydrate-bearing sediments from Gulf of Mexico Green Canyon Block 955, including assessments of geomechanical viscous behavior and NMR permeability. AAPG Bull. https://doi.org/10.1306/04272120204

Yun TS, Santamarina JC, Ruppel C (2007) Mechanical properties of sand, silt, and clay containing tetrahydrofuran hydrate. J Geophys Res 112:B04106. https://doi.org/10.1029/2006JB004484

Publisher's Note